Contract Information

Contract Number	N00014-02-1-0192
Title of Research	Solid Acid Based Fuel Cells
Principal Investigator	Sossina M. Haile
Organization	California Institute of Technology

Technical Section

Technical Objectives

The objectives of this research are to (1) synthesize new solid acid compounds with high proton conductivity that are stable under fuel cell conditions, and (2) develop processing methodologies that lead to high performance membrane-electrode-assemblies (MEAs) based on solid acid compounds. Ultimately, solid acid electrolytes may solve many of the problems facing state-of-the-art polymer based fuel cells. These problems include inoperability at temperatures above 100ºC (which would otherwise increase the CO tolerance of the Pt catalyst), demanding humidification requirements, and methanol permeation across the electrolyte. This work thus aims to simplify fuel cell operation by use of alternative electrolytes.

Technical Approach

The approach we have taken for the synthesis of stable, high-conductivity solid acid compounds derives from the recognition that degradation of materials such as $CsHSO_4$ occurs via the reduction of sulfur under hydrogen to yield H_2S. This reduction reaction is normally slow, even at fuel cell operation temperatures of ~150ºC. However, it is highly accelerated in the presence of typical fuel cell catalysts. By replacing the S (or Se) of superprotonic solid acids with elements such as P, As, Si and Ge, which have greater affinities to oxygen, we anticipate that the reduction reaction will be avoided. Thus, target analogs to $CsHSO_4$ are $BaHPO_4$ and $LaHSiO_4$, *etc*. An additional benefit of such compounds, in cases where alkaline earth or rare earth metals are incorporated rather than alkali metals, is that the resultant compound is water insoluble. In cases where alkali metals are utilized, new stoichiometries such as $Cs_2H_2SiO_4$ can be probed.

In general, acid silicates and germanates are more difficult to synthesize than the analogous sulfates and phosphates, both because of the insolubility of the former group of compounds in water (typically), and because of their tendency to form polymerized structures (with Si-O-Si or Ge-O-Ge linkages) rather than crystallize with isolated XO_4 groups. Our strategy has thus begun with the synthesis of known acid silicates and germanates. Most such compounds contain small alkali ion or alkaline earth ion species, and thus at the outset it was not anticipated that they would exhibit particularly high ionic conductivities or superprotonic phase transitions. In order to prepare crystalline compounds incorporating large cations (which appear necessary for high proton conductivity) we simply follow similar synthesis procedures, but

REPORT DOCUMENTATION PAGE

The public reporting burden for this collection of information is estimated to average 1 hour per response, including the time for reviewing instructions, searching existing data sources, gathering and maintaining the data needed, and completing and reviewing the collection of information. Send comments regarding this burden estimate or any other aspect of this collection of information, including suggestions for reducing the burden, to Department of Defense, Washington Headquarters Services, Directorate for Information Operations and Reports (0704-0188), 1215 Jefferson Davis Highway, Suite 1204, Arlington, VA 22202-4302. Respondents should be aware that notwithstanding any other provision of law, no person shall be subject to any penalty for failing to comply with a collection of information if it does not display a currently valid OMB control number.
PLEASE DO NOT RETURN YOUR FORM TO THE ABOVE ADDRESS.

1. REPORT DATE *(DD-MM-YYYY)*	2. REPORT TYPE	3. DATES COVERED *(From - To)*

4. TITLE AND SUBTITLE

5a. CONTRACT NUMBER

5b. GRANT NUMBER

5c. PROGRAM ELEMENT NUMBER

6. AUTHOR(S)

5d. PROJECT NUMBER

5e. TASK NUMBER

5f. WORK UNIT NUMBER

7. PERFORMING ORGANIZATION NAME(S) AND ADDRESS(ES)

8. PERFORMING ORGANIZATION REPORT NUMBER

9. SPONSORING/MONITORING AGENCY NAME(S) AND ADDRESS(ES)

10. SPONSOR/MONITOR'S ACRONYM(S)

11. SPONSOR/MONITOR'S REPORT NUMBER(S)

12. DISTRIBUTION/AVAILABILITY STATEMENT

13. SUPPLEMENTARY NOTES

14. ABSTRACT

15. SUBJECT TERMS

16. SECURITY CLASSIFICATION OF:			17. LIMITATION OF ABSTRACT	18. NUMBER OF PAGES	19a. NAME OF RESPONSIBLE PERSON
a. REPORT	b. ABSTRACT	c. THIS PAGE			19b. TELEPHONE NUMBER *(Include area code)*

INSTRUCTIONS FOR COMPLETING SF 298

1. REPORT DATE. Full publication date, including day, month, if available. Must cite at least the year and be Year 2000 compliant, e.g. 30-06-1998; xx-06-1998; xx-xx-1998.

2. REPORT TYPE. State the type of report, such as final, technical, interim, memorandum, master's thesis, progress, quarterly, research, special, group study, etc.

3. DATES COVERED. Indicate the time during which the work was performed and the report was written, e.g., Jun 1997 - Jun 1998; 1-10 Jun 1996; May - Nov 1998; Nov 1998.

4. TITLE. Enter title and subtitle with volume number and part number, if applicable. On classified documents, enter the title classification in parentheses.

5a. CONTRACT NUMBER. Enter all contract numbers as they appear in the report, e.g. F33615-86-C-5169.

5b. GRANT NUMBER. Enter all grant numbers as they appear in the report, e.g. AFOSR-82-1234.

5c. PROGRAM ELEMENT NUMBER. Enter all program element numbers as they appear in the report, e.g. 61101A.

5d. PROJECT NUMBER. Enter all project numbers as they appear in the report, e.g. 1F665702D1257; ILIR.

5e. TASK NUMBER. Enter all task numbers as they appear in the report, e.g. 05; RF0330201; T4112.

5f. WORK UNIT NUMBER. Enter all work unit numbers as they appear in the report, e.g. 001; AFAPL30480105.

6. AUTHOR(S). Enter name(s) of person(s) responsible for writing the report, performing the research, or credited with the content of the report. The form of entry is the last name, first name, middle initial, and additional qualifiers separated by commas, e.g. Smith, Richard, J, Jr.

7. PERFORMING ORGANIZATION NAME(S) AND ADDRESS(ES). Self-explanatory.

8. PERFORMING ORGANIZATION REPORT NUMBER. Enter all unique alphanumeric report numbers assigned by the performing organization, e.g. BRL-1234; AFWL-TR-85-4017-Vol-21-PT-2.

9. SPONSORING/MONITORING AGENCY NAME(S) AND ADDRESS(ES). Enter the name and address of the organization(s) financially responsible for and monitoring the work.

10. SPONSOR/MONITOR'S ACRONYM(S). Enter, if available, e.g. BRL, ARDEC, NADC.

11. SPONSOR/MONITOR'S REPORT NUMBER(S). Enter report number as assigned by the sponsoring/ monitoring agency, if available, e.g. BRL-TR-829; -215.

12. DISTRIBUTION/AVAILABILITY STATEMENT. Use agency-mandated availability statements to indicate the public availability or distribution limitations of the report. If additional limitations/ restrictions or special markings are indicated, follow agency authorization procedures, e.g. RD/FRD, PROPIN, ITAR, etc. Include copyright information.

13. SUPPLEMENTARY NOTES. Enter information not included elsewhere such as: prepared in cooperation with; translation of; report supersedes; old edition number, etc.

14. ABSTRACT. A brief (approximately 200 words) factual summary of the most significant information.

15. SUBJECT TERMS. Key words or phrases identifying major concepts in the report.

16. SECURITY CLASSIFICATION. Enter security classification in accordance with security classification regulations, e.g. U, C, S, etc. If this form contains classified information, stamp classification level on the top and bottom of this page.

17. LIMITATION OF ABSTRACT. This block must be completed to assign a distribution limitation to the abstract. Enter UU (Unclassified Unlimited) or SAR (Same as Report). An entry in this block is necessary if the abstract is to be limited.

change one or more of the reactant materials, for example replacing NaOH to CsOH to yield a cesium acid silicate or germanate. A second approach to large cation silicates and germanates is to carry out ion exchange reactions on known compounds. That is, we can, replace the Na in a known acid silicate with Cs by soaking in molten CsOH. A third approach is to prepare compounds containing Li rather than H, and then perform ion exchange experiments in acid media. For example, the compound $LaLiSiO_4$ is known, and it may be possible to replace the lithium with protons using an acid that will not dissolve the base material.

Because of the challenges encountered in the synthesis of acid silicates and germanates, efforts have also been directed towards phosphate (and arsenate) compounds, which combine the benefits of chemical stability, resistance to anion group polycondensation, and, when prepared with the appropriate cation, water insolubility. Specifically, we have pursued acid phosphate (and arsenate) analogs to $Rb_3H(SeO_4)_2$, a known superprotonic conductor. This selenate undergoes a transition from a monoclinic, pseudo-trigonal phase to a trigonal one at ~180°C. Similar behavior is exhibited by several other selenates and sulfates including $Cs_3H(SeO_4)_2$, $(NH_4)_3H(SeO_4)_2$ and $(NH_4)_3H(SO_4)_2$. The hypothesized acid phosphates (and arsenates) have general formula $M'_{3-x}M''_xH_x(XO_4)_2$ where M' is an alkaline earth metal, M'' is an alkali metal and X = P, As. They are particularly attractive because the known compounds $Ba_3(PO_4)_2$ and $Pb_3(PO_4)_2$, although not proton hosts, are isostructural to the selenate in its trigonal, superprotonic phase [U. Bismayer, E. Salje, *Acta Cryst.* **A37** (1981) 145-153]. Thus, our focus has been on replacing a portion of the M^{2+} cations with pairs of M^+ and H^+ species so as to incorporate mobile protons.

In the arena of MEA processing, we have focused on the fabrication of thin-film CsH_2PO_4-based fuel cells with high power densities. Although this material is a well-known compound, we had not initially considered it for use as a fuel cell electrolyte because its superprotonic phase transition (at ~ 230°C) is nearly commensurate with dehydration. However, investigation of the thermodynamic properties of CsH_2PO_4, under a related NSF-sponsored program, has revealed that the superprotonic phase can be stabilized (with respect to dehydration) up to 300°C by only 0.5 atm partial pressure of water, equivalent to the vapor pressure of water at roughly 80°C. CsH_2PO_4 is furthermore stable against reduction, even in the presence of Pt catalyst at the anode (in contrast to sulfate or selenate based solid acids, which are readily reduced and evolve H_2S or H_2Se). The variety of processing approaches pursued are too numerous to document here. Instead, we report the fabrication route that was employed to successfully prepare fuel cells with 25-40 μm thick membranes and power densities as high as 415 mW/cm^2.
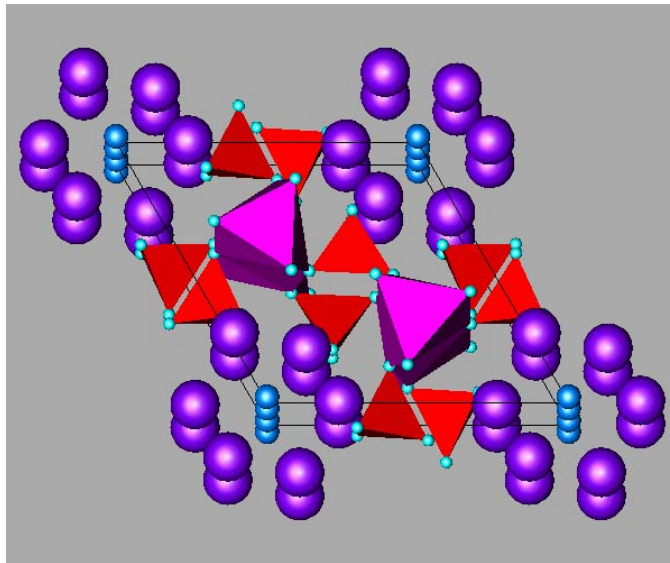
Accomplishments

Stable Solid Acids

$LiLa_9(SiO_4)_6O_2$ and its proton-exchanged analog

The structure of the compound designated 'LaLiSiO$_4$' silicate was recently reported by Sato *et al*. [M. Sato, Y. Kono, H. Ueda, K. Uematsu and K. Toda, *Solid State Ionics* **83** (1996) 249-256], who utilized X-ray powder diffraction to determine the atomic positions. These authors concluded that the bulk material consisted of an apatite phase (hexagonal symmetry) of variable composition, $Li_xLa_{10-x}(SiO_4)_6O_{3-x}$, with excess lithium residing in the grain boundaries of polycrystalline pellets to yield the nominal composition LaLiSiO$_4$. By slow cooling of solid state reaction synthesized material ($Li_2CO_3 + La_2O_3 + SiO_2$ at 1000°C/10hr), we have obtained crystals large enough for single crystal X-ray diffraction studies. Our results, summarized in Tables 1 and 2, indicate that this compound is a rather conventional apatite with fixed stoichiometry, $LiLa_9(SiO_4)_6O_2$ (x = 1). Such a result is, indeed, not surprising because it is precisely at this stoichiometry that the O atom sites are fully occupied. It is particularly unlikely that x could be less than 1 as there is no place for excess oxygen within the structure, Figure 1.

Ion exchange, to replace the Li+ in $LiLa_9(SiO_4)_6O_2$ with H+ was typically carried by exposing the silicate to a strong mineral acid (HCl, H_2SO_4 or H_3PO_4) under a variety of conditions. The experimental procedures and results are summarized in Table 3. While amorphous gels/powders, were obtained from H_2SO_4 and HCl (and this result was obtained for a number of silicates), a crystalline product was obtained when the exchange medium was phosphoric acid. This observation suggests that the combination of rare earth element in the silicate and relatively weak acid for exchange provides a useful route for avoiding dissolution/gelation of the precursor material.

In order to establish whether Li → H exchange indeed occurred in $LiLa_9(SiO_4)_6O_2$ as a result of thermal treatment in phosphoric

Figure 1. Structure of $LiLa_9(SiO_4)_6O_2$ shown in projection along a direction close to [0 0 1] (the *c*-axis). Red tetrahedral group are SiO$_4$ units, oxygen atoms shown at the corners; pink octahedral groups are occupied by both La (¾ of the sites) and Li (¼ of the sites); large purple atoms are lanthanum, and small blue atoms are oxygen atoms not bonded to silicon and residing in channels that extend along *c*. The octahedral [(La,Li)O$_6$] groups are also arranged along a channel extending along

acid, several experiments were carried out comparing the as-synthesized and post-exchange materials including X-ray powder diffraction, ^{1}H MAS NMR (magic angle spinning, nuclear magnetic resonance

spectroscopy), ^{7}Li MAS NMR, and thermogravimetric analysis. The X-ray diffraction patterns are presented in Figure 2. It is evident that upon exposure to phosphoric acid, some changes in the structure occur, reflected in changes in peak in intensities and peak splitting, but that the basic structural features remain the same.

Table 1. Crystallographic data, data collection parameters, and data refinement parameters for the structure determination of $LiLa_9(SiO_4)_6O_2$.

_____

Crystal Data

Formula weight	1841.67
Crystal system	Hexagonal
Space group	$P6_3/m$
Unit cell dimensions	a = 9.690(6) Å
	c = 7.150(6) Å
Volume	581.4(8) $Å^3$
Z	1
Density (calculated)	5.216 g/cm^3

Data Collection

Radiation	X-ray, MoKα, 0.71070 Å
Θ range for data collection	2.4 to 30.0°
Index ranges	$0 \leq h \leq 12$, $-2 \leq k \leq 11$, $-2 \leq l \leq 10$
Reflections collected	1144

Refinement

Final R indices [I>2σ(I)]	R1 = 0.0317
R indices (all data)	R1 = 0.0340, wR2 = 0.0770
Goodness-of-fit on F^2	1.129
Reflections used in refinement	610
Refined parameters	44

_____

Table 2. Atomic coordinates and equivalent isotropic displacement parameters ($Å^2$) for $LiLa_9(SiO_4)_6O_2$. U(eq) is defined as one third of the trace of the orthogonalized Uij tensor.

_____

Atom	x	y	z	Occ	U(eq)
La(1)	-0.24571(5)	-0.23106(5)	0.25	1	0.00590(22)
La(2)	0.66667	0.33333	0.00226(13)	0.75	0.0115(3)
Li	0.66667	0.33333	0.05(6)	0.25	n/a
Si	0.40208(23)	0.37231(24)	0.25	1	0.0049(4)
O(1)	0.5957(7)	0.4724(7)	0.25	1	0.0197(14)
O(2)	0.3247(8)	0.4868(7)	0.25	1	0.0137(11)
O(3)	0.3437(8)	0.2541(6)	0.0685(7)	1	0.0270(12)
O(4)	0	0	0.25	1	0.0174(23)

_____

Table 3. Experimental conditions and results of ion exchange experiments.

Compound	Acid	Environment	Period, days	Product
LiLa$_9$(SiO$_4$)$_6$O$_2$	H$_2$SO$_4$	Thermal bomb, 250°C	2	Amorphous
LiLa$_9$(SiO$_4$)$_6$O$_2$	HCl	Thermal bomb, 250°C	3	Amorphous
LiLa$_9$(SiO$_4$)$_6$O$_2$	HCl	Continuous stirring, 25°C	2	Amorphous
LiLa$_9$(SiO$_4$)$_6$O$_2$	H$_3$PO$_4$	Thermal bomb, 250°C	2	**Crystalline**
LiLa$_9$(SiO$_4$)$_6$O$_2$	H$_3$PO$_4$	Thermal bomb, 250°C	4	**Crystalline**
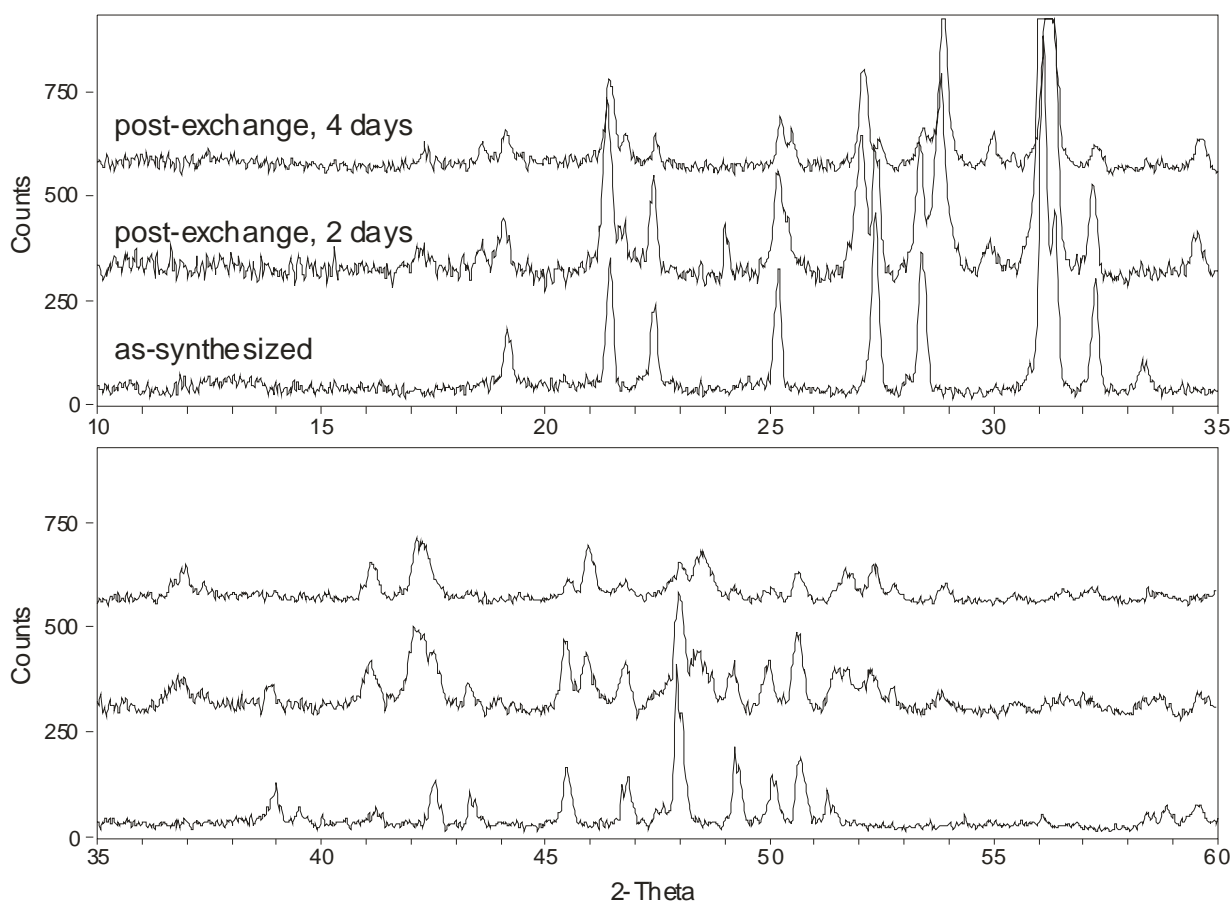
Figure 2. X-ray powder diffraction patterns of as-synthesized and post-exchange (2 and 4 days) LiLa$_9$(SiO$_4$)$_6$O$_2$.

Convincing evidence for successful ion exchange comes from the NMR data. The proton NMR results, Figure 3, show that the as-synthesized material contains essentially no protons, and that with increasing exposure to phosphoric acid, the proton content increases. Note that the intensity scale is normalized to the total mass of material. The data further indicate that there are two different sites for proton incorporation, the first with a clear chemical shift of ~ 8.9 ppm, and the second with a shift of anywhere from 5.5 to 6.9 ppm. Greater chemical shifts typically reflect stronger hydrogen bonding,

whereas smaller shifts reflect weaker bonds and possible proton incorporation on the sample surface or grain boundary region.

In good agreement with the proton NMR studies, the lithium NMR results, Figure 4, show that with increasing exposure to phosphoric acid the Li content in $LiLa_9(SiO_4)_6O_2$ monotonically decreases. Here too, multiple Li sites in the structure are apparent from the multiple NMR peaks. In the case of the as-synthesized material, the shifts of ~ 0.95 and -1.1 ppm are suggestive of 3-fold and 6-fold coordinated Li, respectively [J.F. Stebbins, *Solid State Ionics* **112** (1998) 137-141]. Within the apatite structure, the La(2) and Li atoms are both located within a octahedron formed of oxygen ions, with La occupying ¾ of the possible octahedra and Li occupying the remaining ¼. The lithium ion is rather small for octahedral coordination, and our X-ray structure analysis suggests that, rather than remaining centrally located within the octahedron, it pulls over to one side such that it has three near oxygen neighbors and another three that are more distant. If such displacement occurs only for some portion of the Li, then one can readily interpret the NMR data for the as-synthesized material. Upon ion exchange, the intensities of both the 0.95 and -1.1 ppm peaks decrease dramatically, and a new peak at close to 0 ppm appears. A shift of 0 is suggestive of a 4-fold coordinated Li atom, but, again, complete resolution of the location of this site will await single crystal studies.
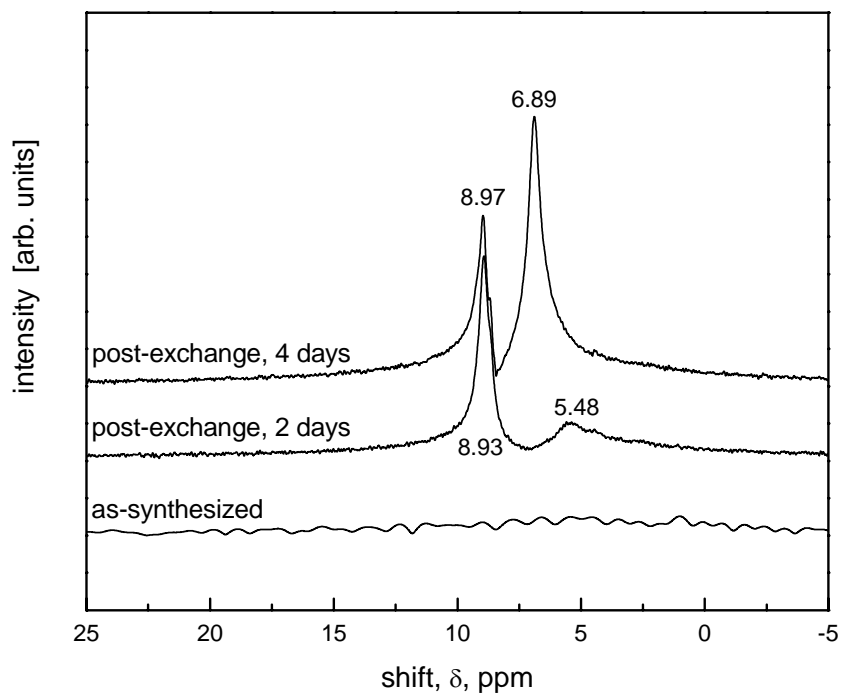

Figure 3. ^1H MAS NMR spectra of as as-synthesized and post-exchange (2 and 4 days) $LiLa_9(SiO_4)_6O_2$, as referenced to TMS (tetramethyl silane).
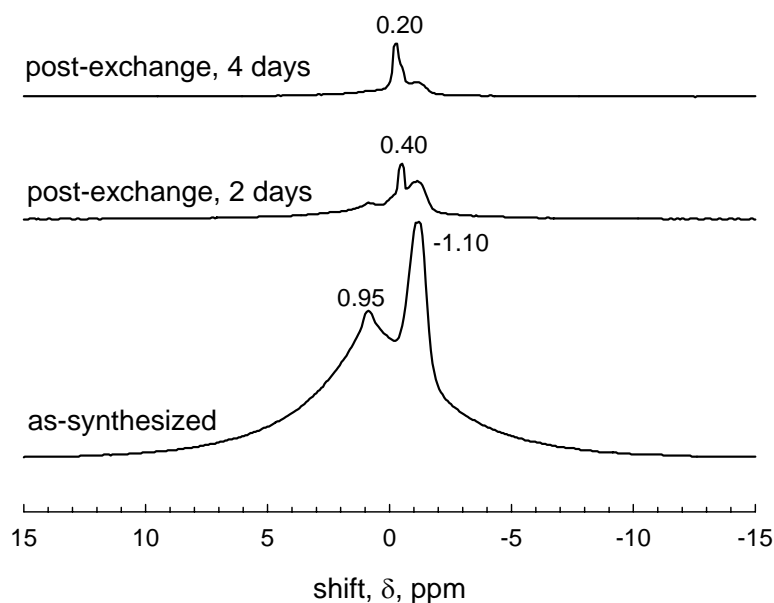
**Figure 4.** ^{7}Li MAS NMR spectra of as as-synthesized and post-exchange (2 and 4 days) LiLa$_9$(SiO$_4$)$_6$O$_2$, as referenced to 1.0 M LiCl in aqueous solution.

The thermogravimetric data, Figure 5, further confirm that proton exchange has been achieved. In the case of the as-synthesized material, a small weight loss of 0.25 wt% is evident over the temperature range 80 to 800C, whereas the post-exchange material exhibits a total weight loss of 1.3 wt% (or 1.05 wt% more than the as-synthesized material). This value is somewhat great than the 0.49 wt% expected for the dehydration of fully protonated material, HLa$_9$(SiO$_4$)$_6$O$_2$, to form La$_9$(SiO$_4$)$_6$O$_{1.5}$ and suggests additional modes of proton and/or water incorporation, perhaps on the crystallite surfaces.
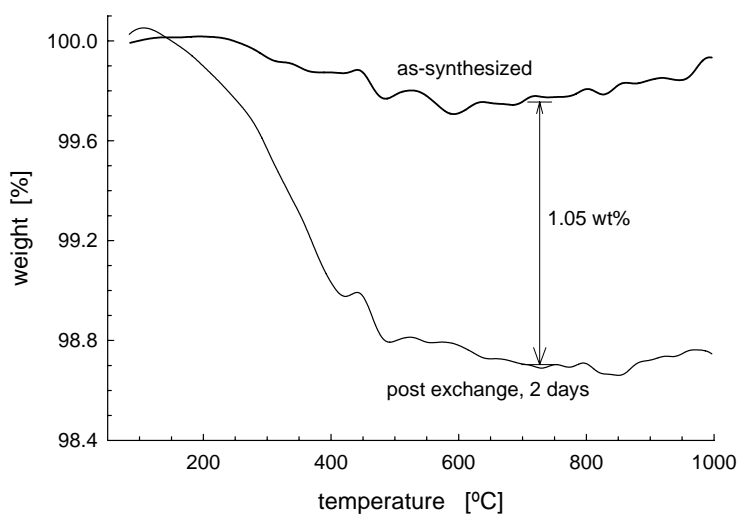
Figure 5. Thermal gravimetric traces of as-synthesized and post-exchange (2 days) LiLa$_9$(SiO$_4$)$_6$O$_2$. [Netzsch STA 449, 20ºC/min, flowing Ar at 40 cc/min].

In Figure 6, the conductivity of the post exchange (2-day) sample shows that the presence of protons increased the conductivity of the compound by several orders of magnitude compared to the fully lithiated compound. The exchanged sample's conductivity increases until around 200°C, after which it starts to slowly decrease. This behavior agrees with the thermogravimetric analysis (Figure 5) that showed significant weight loss for the 2-day exchanged sample to start around 200°C. The exchange of lithium ions for protons then dramatically increases the conductivity of this compound, even though it retains the ordered apatite structure.
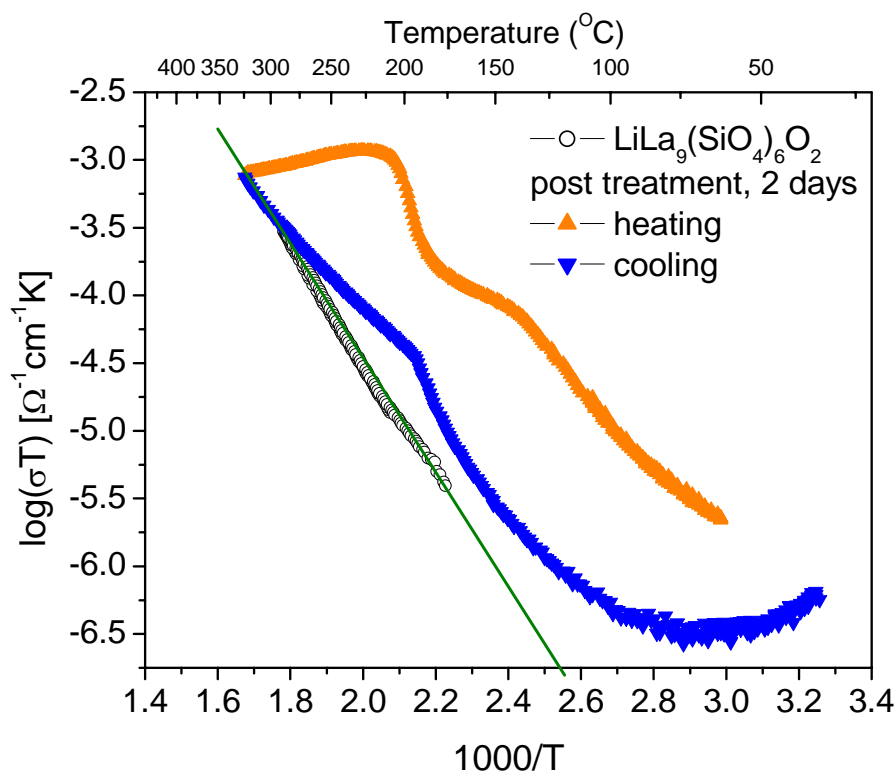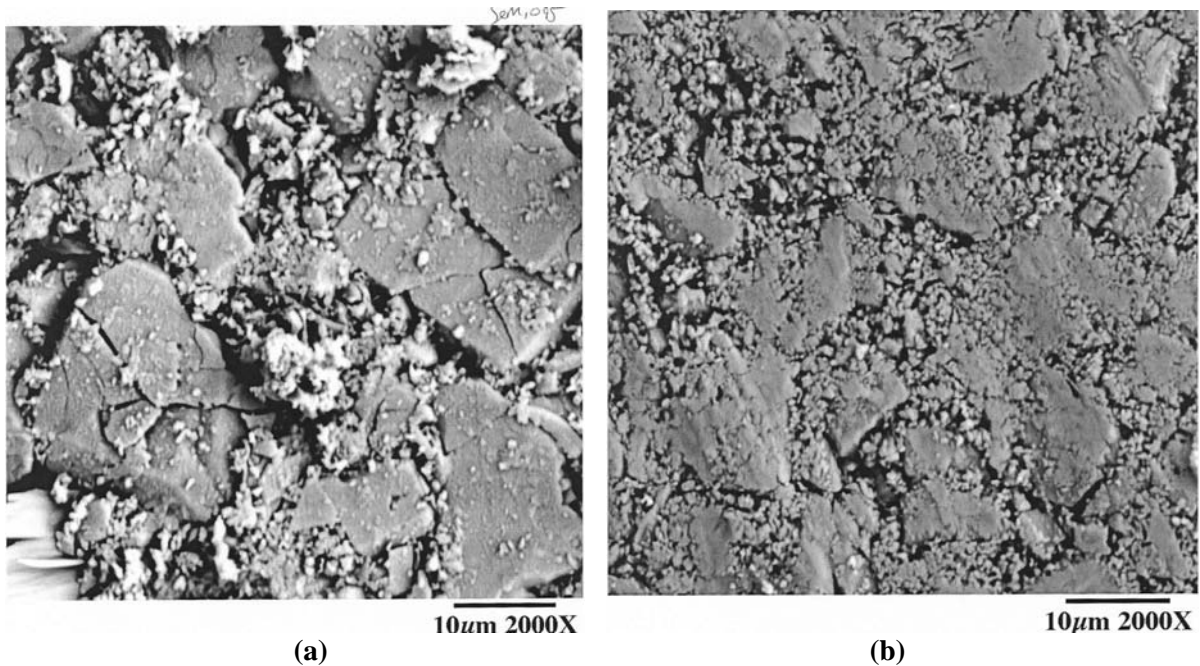

Figure 6. Conductivity of $LiLa_9(SiO_4)_6O_2$ and post exchange (2 days) pressed powder pellets in Arrhenius plots. Measurements taken in air at heating/cooling rates of 0.5°C/min with painted silver electrodes.
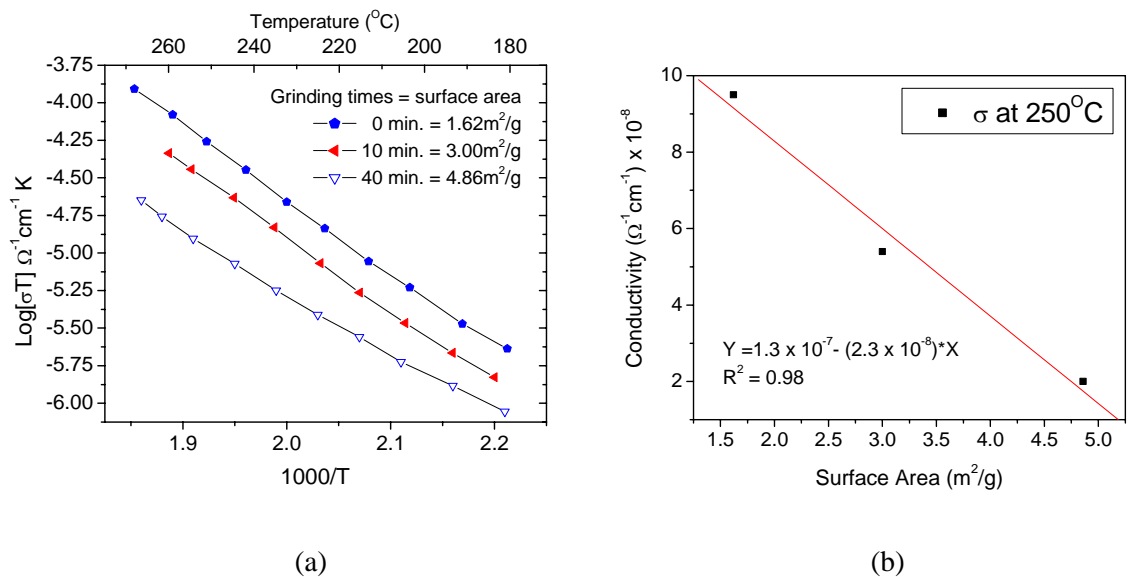
NaCaHSiO₄

The compound $NaCaHSiO_4$ is one of just a handful of known acid silicates with isolated SiO_4 groups. It was synthesized here by mild hydrothermal methods. NaOH, $Ca(OH)_2$ and SiO_2 were placed in a 3:2:2 molar ratio along with a few drops of water in a thermal bomb, then held at 250°C for ~ 72 hours. The conductivity of this material is, unlike sulfate and phosphate solid acids, dominated by its grain boundary properties, with *larger* grained polycrystalline samples resulting in overall *higher* conductivities. The particle size of powders subsequently used in pressing pellets was varied simply by mechanical milling,

Figure 7, and the specific surface areas measured by nitrogen adsorption (BET) methods. As can be seen in Figure 8a, the conductivity of $NaCaHSiO_4$ pressed powder pellets decreases with increasing grinding/surface area.

(a)   **(b)**

Figure 7. Scanning electron micrographs of $NaCaHSiO_4$ (a) as synthesized and (b) after 10 minutes of mechanical grinding.

(a)   (b)

Figure 8. Conductivity measurements for $NaCaHSiO_4$ pressed powder pellet samples (a) in Arrhenius plots and (b) at 250°C showing the effect of grinding time/surface area. Measurements taken in argon at heating/cooling rates of 0.5°C/min with painted silver electrodes.

In Figure 8 b, the dependence of the total conductivity at 250°C of $NaCaHSiO_4$ on surface area have been fit to a line; the bulk conductivity is estimated to be the value at which this line crosses the y-axis. Such an approximation gives a bulk conductivity of 1.3 x 10^{-7} $\Omega^{-1}cm^{-1}$ at 250°C. This value is about an order of magnitude less than 1.1 x 10^{-6} and 3.4 x 10^{-6} $\Omega^{-1}cm^{-1}$, the conductivities of $CsHSO_4$ (at 130°C) and CsH_2PO_4 (at 220°C), respectively, just below their superprotonic phase transitions. Also, calculating the activation energies for proton transport from the slopes of the curves in Figure 1, one gets an average value of 0.9 eV. This value can be compared to activations energies of 0.67 and 0.74 eV for $CsHSO_4$ and CsH_2PO_4, respectively, in their room temperature phases. The estimated bulk conductivity and activation energy values for $NaCaHSiO_4$ therefore support the assumption that the smaller cations and increased electrostatic bonding will inhibit proton conduction (leading to smaller overall conductivities and larger activation energies) when compared to large metal cation sulfate and phosphate solid acids. These insights provide guidance as to the crystal chemical modifications required to enhance the conductivity of acid silicates analogous to $NaCaHSiO_4$.

$M'_{3-x}M''_xH_x(XO_4)_2$ Compounds

Several target $M'_{3-x}M''_xH_x(XO_4)_2$ compounds were pursued by several different synthesis routes. Of these, synthesis of $Ba_{3-x}K_xH_x(PO_4)_2$, via a route analogous to that reported for the preparation of $K_3CaH(PO_4)_2$ [A.W. Frazier, J.P. Smith, W.E. Brown, J.R. Lehr; *INORGANIC CHEMISTRY* **1** (1962) 949-951], was most successful, Table 4. In general, an aqueous solution of the alkaline earth acetate $[M' (CH_3COO)_2]$ was slowly added to a second aqueous solution containing both the alkali acid phosphate (M''_2HPO_4) and the alkali hydroxide (M''OH). Rapid stirring during the addition (30 minutes) promoted formation of a uniform gel, which crystallized after standing 1 to 3 hr at room temperature; samples were typically allowed to set for a total of 2 days beyond the initial crystallization period. The resulting crystallites were collected, washed several times with water, then once with acetone, and subsequently dried at 75°.

X-ray powder diffraction of the products from syntheses 1-3, Figure 9, showed that the target trigonal phase, $Ba_{3-x}K_xH_x(PO_4)_2$, has indeed been obtained. The crystallite morphology, Figure 10, is also consistent with the phase identification as trigonal. Furthermore, the compound is insoluble in water, as anticipated.

Careful examination of the diffraction data obtained from syntheses 1-3 showed a clear variation in cell parameters with synthesis conditions, which was hypothesized to result from differences in stoichiometry. Accordingly, the materials were further examined by EDS (energy dispersive spectroscopy) chemical analysis, (using internal standards), thermal gravimetric analysis (TGA), and ^{1}H magic angle spinning NMR spectroscopy, to establish K, B and H contents.

Table 4. Synthesis conditions and results for various mixed $Ba_{3-x}M_xH_x(XO_4)_2$ compounds. Synthesis number refers to route described in the text.

| Syn.	Desired Compound	Reagents	pH	Synthesis Modification	Product
#1	$Ba_{3-x}K_xH_x(PO_4)_2$	1)K_2HPO_4 + KOH 2)$Ba(CH_3COO)_2$	12.5	Baseline reagent concentrations 120 min stirring, 12 hours soak in soln	$Ba_{3-x}K_xH_x(PO_4)_2$
#2	$Ba_{3-x}K_xH_x(PO_4)_2$	1)K_2HPO_4 + KOH 2)$Ba(CH_3COO)_2$	12.5	½ Ba content of synthesis #1 10 min stirring, 12 hours soak in soln.	$Ba_{3-x}K_xH_x(PO_4)_2$
#3	$Ba_{3-x}K_xH_x(PO_4)_2$	1)K_2HPO_4 + KOH 2)$Ba(CH_3COO)_2$	12.5	Baseline reagent concentrations	$Ba_{3-x}K_xH_x(PO_4)_2$
#4	$Ba_{3-x}Na_xH_x(PO_4)_2$	1)Na_2HPO_4 + NaOH 2)$Ba(CH_3COO)_2$	14	Baseline reagent concentrations	$NaBaPO_4$
#5	$Ba_{3-x}Na_xH_x(PO_4)_2$	1)Na_2HPO_4 + NaOH +H_3PO_4 2)$Ba(CH_3COO)_2$	12.5	Baseline reagent concentrations	$NaBaPO_4$
#6	$Ba_{3-x}(NH_4)_xH_x(PO_4)_2$	1)$(NH_4)_2HPO_4$ + NH_4OH 2)$Ba(CH_3COO)_2$	14	Baseline reagent concentrations	$Ba_3(PO_4)_2$ + $BaHPO_4$
#7	$Ba_{3-x}(NH_4)_xH_x(PO_4)_2$	1)$(NH_4)_2HPO_4$ + NH_4OH +H_3PO_4 2)$Ba(CH_3COO)_2$	12.5	Baseline reagent concentrations	$Ba_3(PO_4)_2$ + $BaHPO_4$
#8	$Ba_{3-x}K_xH_x(AsO_4)_2$	1)$H_5As_3O_{10}$ + KOH 2)$Ba(CH_3COO)_2$	11	Baseline reagent concentrations	$Ba_3(AsO_4)_2$
#9	$Ba_{3-x}K_xH_x(AsO_4)_2$	1)$H_5As_3O_{10}$ + KOH 2)$Ba(CH_3COO)_2$	12.5	Baseline reagent concentrations	$Ba_3(AsO_4)_2$

A clear correlation between cell volume and potassium content is evident, Figure 11, indicating that the compound $Ba_{3-x}K_xH_x(PO_4)_2$ has indeed been obtained and that its stoichiometry can be varied over a measurable range. The TGA curves, Figure 12(a), show a smooth weight loss for all three samples, with the greatest weight change occurring for the sample with the greatest potassium content, as expected. However, the weight loss is greater than that implied by the stoichiometry by chemical analysis. Specifically, assuming the dehydration reaction of Eq. (1)

$$Ba_{3-x}K_xH_x(PO_4)_2 \rightarrow (1-x/3)Ba_3(PO_4)_2 \text{ (s)} + (x/3)K_3PO_4 \text{ (s)} + (x/6)P_2O_5 \text{ (s)} + (x/2)H_2O \text{ (g)} \quad (1)$$

and that only water is lost, the hydrogen and potassium contents of the compounds, x, can be determined. The value of x so established from the TGA experiments is about 65% greater than that measured directly
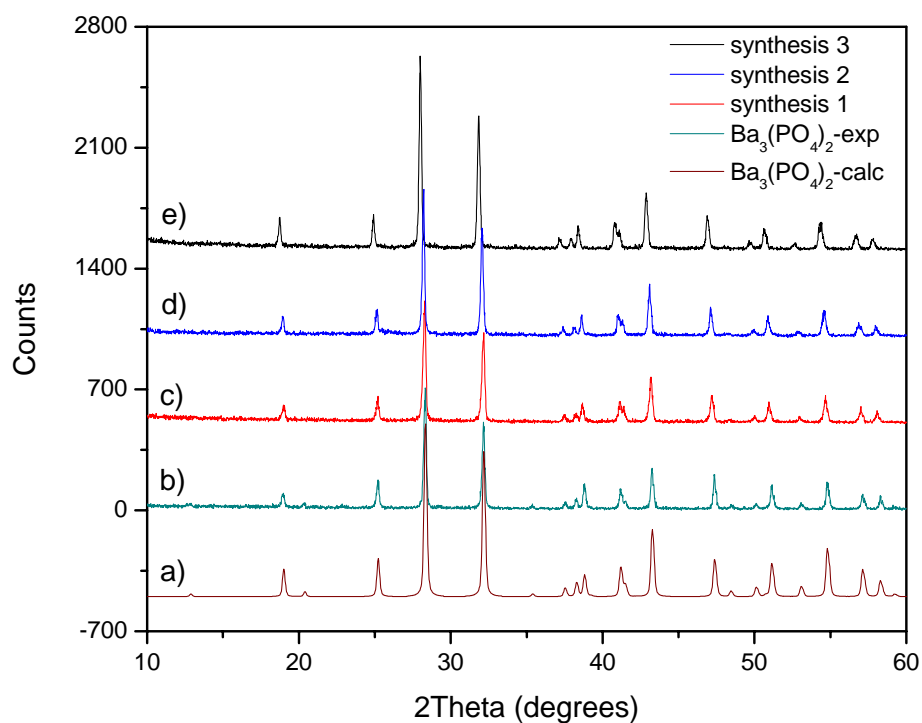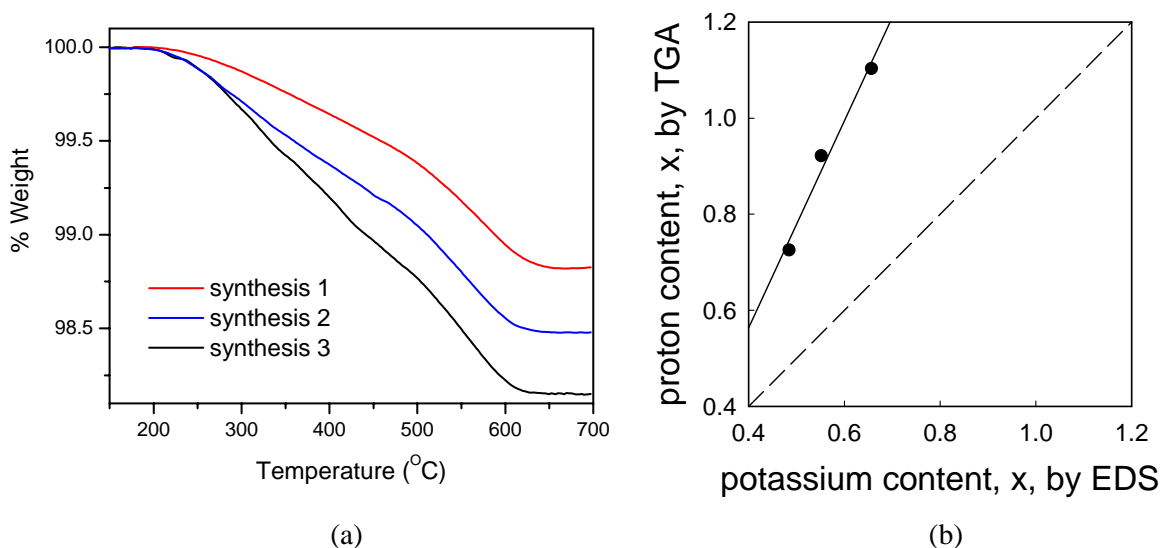
Figure 9. Powder X-ray diffraction patterns for (a) the reported structure of trigonal $Ba_3(PO_4)_2$, (b) in-house synthesized $Ba_3(PO_4)_2$, and (c-e) the product material $[Ba_{3-x}K_xH_x(PO_4)_2]$ from syntheses 1-3, respectively.
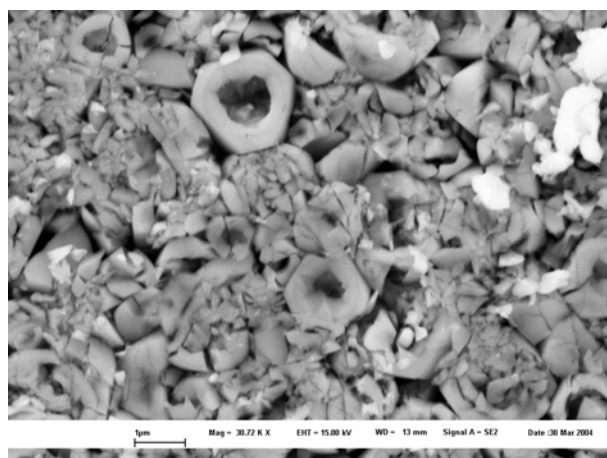
Figure 10. SEM image of product of synthesis 1.
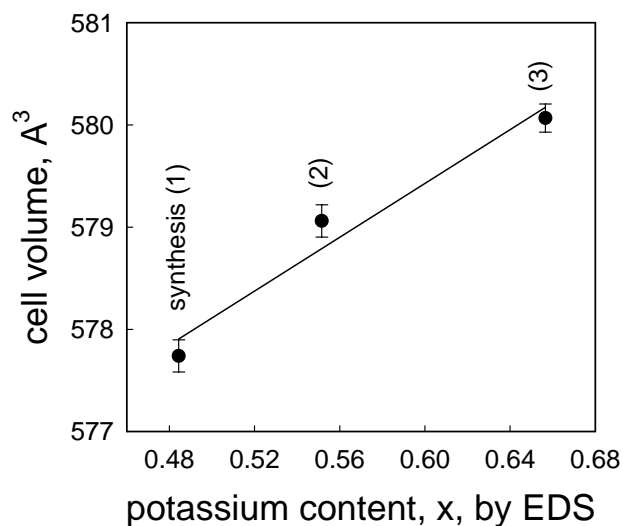
**Figure 11**. Correlation between unit cell volume and potassium content.

Figure 12. (a) TGA curves obtained from $Ba_{3-x}K_xH_x(PO_4)_2$ and (b) correlation between proton content implied by total weight loss, Eq. 1, and potassium content. Dotted line in (b) is expected correlation based on the assumed stoichiometry of the compound.

maximum value of $x = 1$ is expected on the basis of structural considerations. The discrepancy between the TGA and EDS measurements is likely due to additional weight loss in the thermogravimetric experiments as a result of volatilization of surface adsorbed water and/or phosphorous containing species. Thermal analysis in conjunction with off-gas analysis via mass spectrometry is currently underway to resolve this outstanding question.

The H^+ NMR magic angle spinning (MAS) measurements the revealed two broad peaks centered at ~ 13 and 6 ppm for all three synthesized powders, suggesting the presence of both strongly and weakly bound protons, respectively, in the $Ba_{3-x}K_xH_x(PO_4)_2$ compounds, Figure 5(a). Using $Rb_3H(SeO_4)_2$ as a reference, the integral intensities under the peaks were used to calculate the hydrogen content of the compounds. Again, the greatest proton content is observed in the sample with the greatest potassium content, however, once again, the proton content measured by this method is ~ 65% larger than that implied by the EDS measurements, Figure 5(b). This result seems to imply that the weakly bound protons with chemical shift of ~ 6 ppm are due to surface absorbed species, further suggesting that the TGA measurements do indeed include weight loss contributions due to loss of these species. However, preliminary temperature dependent NMR experiments (not shown) indicate that the weakly bound protons are structural rather than surface species. Further NMR studies are anticipated to establish the precise nature of the incorporated protons.

The impact of proton incorporation on the conductivity of barium phosphate (as measured by a.c. impedance spectroscopy under ambient atmospheres) is dramatic, Figure 6. The $Ba_{3-x}K_xH_x(PO_4)_2$

compounds have conductivities that are nearly three orders of magnitude greater than that of simple $Ba_3(PO_4)_2$. Moreover, within the $Ba_{3-x}K_xH_x(PO_4)_2$ series, the conductivity increases with increasing proton content to their decomposition temperatures ~ 200ºC, as one would expect.


(a)   (b)
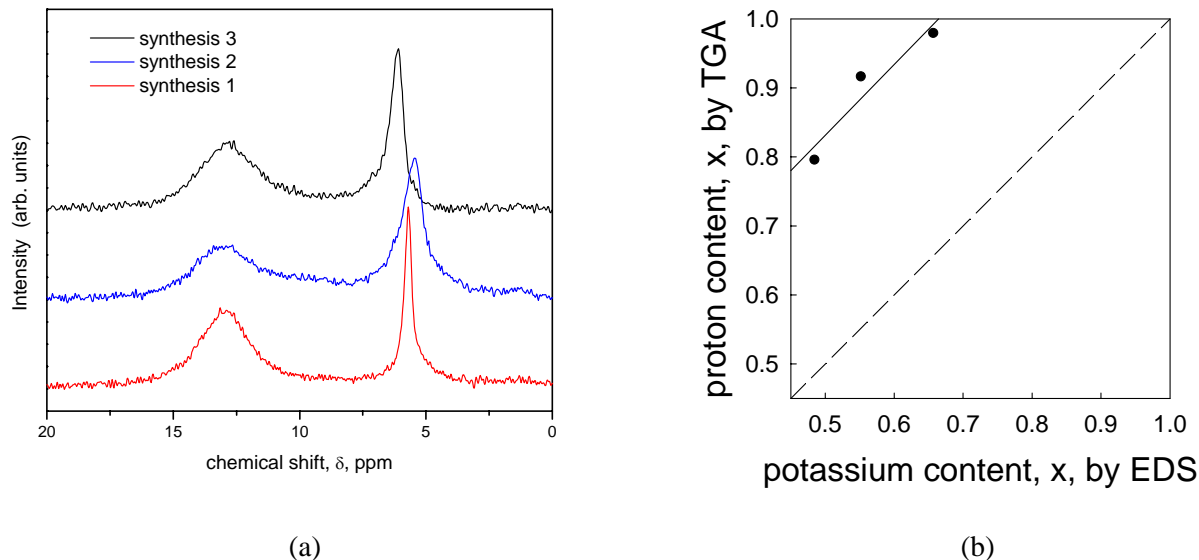
Figure 13. Proton NMR measurements on $Ba_{3-x}K_xH_x(PO_4)_2$ compounds, a), show two distinct types of protons in the compounds with peak positions around 13 and 6 ppm. A plot of the proton content determined by EDS versus NMR measurements, b), shows the two sets of data to have a nearly linear relationship, although the EDS values are ~ 60% of those determined by H^+ NMR.
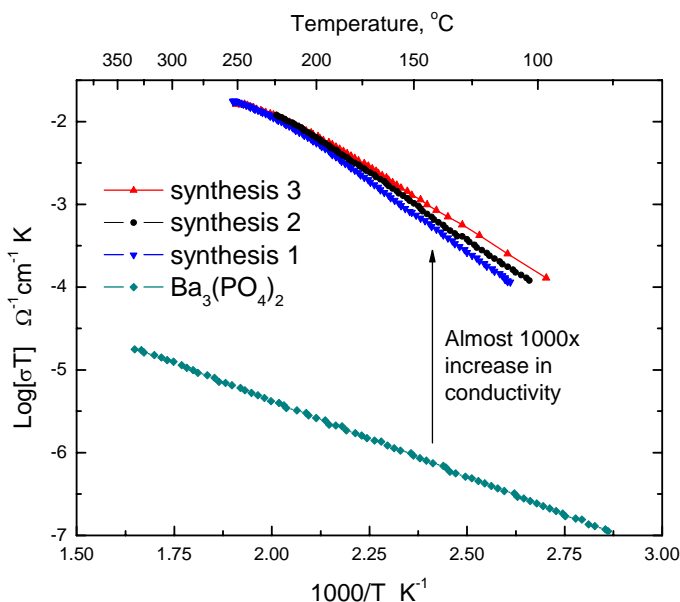
Figure 14. Conductivity of pure $Ba_3(PO_4)_2$ and the three synthesized $Ba_{3-x}K_xH_x(PO_4)_2$ compounds. The potassium/hydrogen containing compounds show nearly a 1000 times increase in their conductivity compared to the undoped sample. Note the conductivity of the doped samples increases with increasing hydrogen/potassium content.

14

While we have thus demonstrated success in hypothesizing and synthesizing new proton conducting materials, it is noteworthy that the conductivity of $Ba_{3-x}K_xH_x(PO_4)_2$ is 2-3 orders of magnitude lower than that of superprotonic $Rb_3H(SeO_4)_2$ and superprotonic phases in general [A. Powlowski, Cz. Pawlaczyk, B. Hilczer, *Solid State Ionics* **44** (1990) 17-19]. Slight differences in the crystal chemistry of $Ba_3(PO_4)_2$ and superprotonic $M_3H(XO_4)_2$ may explain this difference in behavior. In these compounds, the oxyanion groups form hexagonal layers, further combined into bilayers in which apical oxygen atoms of each component layer point towards the other layer. In addition, the two layers are displaced from one another. Cations are located both within the bilayers and in separate layers between those of the oxyanions [A. Bohn et al., *Solid State Ionics* **77** (1995) 111-117]. One such bilayer is shown in projection in Figure 15. In the acid sulfates and selenates, apical oxygen atoms, one from each layer in the bilayer, are tilted towards one another to form hydrogen bonds. In the phosphates (which have no protons), apical oxygen atoms are tilted towards the cations to form M^{2+}-O bonds. In the mixed acid phosphates, it is likely that a competition between hydrogen bond and metal-oxide bond formation occurs and this is responsible for the reduction in proton conductivity relative to sulfates and selenates. Crystal chemical tailoring of the structure via substitutions on the cation and/or oxyanion group sites to favor hydrogen bond formation may result in truly superprotonic acid phosphates.
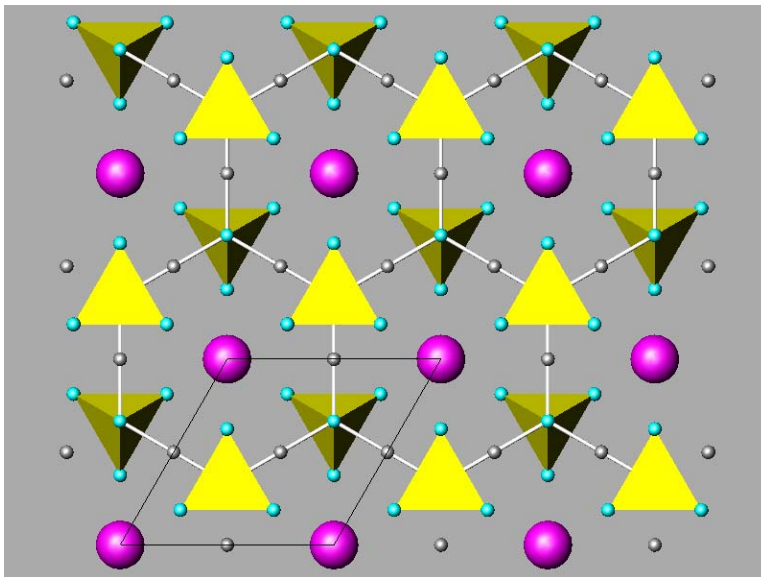
Figure 15. A portion of the structure of $M_3H(XO_4)_2$ shown in projection on the basal plane. Oxyanion tetrahedral groups shown in yellow and cations shown in magenta.

MEAs

The general configuration of our membrane-electrode-assemblies (MEAs), much as in PEM fuel cells, incorporates a solid acid electrolyte (CsH_2PO_4) sandwiched between two electrocatalyst layers, in turn, sandwiched between two porous graphite current collectors or gas diffusion layers. The electrocatalyst

layer typically comprises a mixture of Pt black (or, occasionally, carbon supported Pt), graphite, electrolyte and a volatile organic, typically naphthalene. In order to reduce the electrolyte thickness (which is the primary source of fuel cell voltage drop for membranes >50 μm in thickness), we have most recently pursued a design in which the fuel cell MEA is borne on a porous, conductive support material. Fuel cells, shown schematically in Fig. 16(a), were fabricated using a colloidal deposition process in which the electrolyte, CsH_2PO_4, was suspended in toluene. An electrocatalyst layer, containing a mixture of CsH_2PO_4, naphthalene, Pt black and Pt supported on carbon was deposited onto a porous stainless steel support, which served both as a current collector and a gas diffusion layer, and the two layers then die-pressed together. An electrolyte layer was then deposited onto this bi-layer structure and also pressed. A second electrocatalyst layer was subsequently deposited, followed by placement of the second gas diffusion electrode as the final layer of the 'sandwiched' structure. The ratio of CsH_2PO_4, Pt black, platinum supported on carbon (50 mass% Pt), and naphthalene in the electrocatalyst layer was 3:3:1:0.5 (by mass), giving a Pt content (or 'loading') of 7.7 mg/cm^2 (per electrode). The average pore size and porosity of the porous stainless steel were 40 μm and 42 %, respectively. The electrolyte thickness, as estimated from the quantity of electrolyte used in the deposition step, was 25 μm. Both the electrolyte thickness (25 μm) and the Pt loading (7.7 mg/cm^2) attained here represent substantial advances from our previous report of 260 μm and 18 mg Pt/cm^2, respectively [D. A. Boysen, T. Uda, C. R. I. Chisholm & S. M. Haile, *Science*, **303**, 68 (2004).]. Fuel cell polarization curves were measured using an in-house constructed test station. The cell temperature was maintained at 240 °C, with humidified hydrogen and humidified oxygen (0.3 atm H_2O) supplied to the anode and cathode with flow rate of 200 cc / min, respectively. A total pressure of 1 atm was maintained at both electrodes.

The fuel cell polarization and power output curves, Figure 16(b), show that indeed power output has been limited primarily by electrolyte thickness rather than electrocatalyst behavior. The reduction in membrane thickness by a factor of ~ 10 (from 260 μm to 25 μm) results in an increase in peak power density by a factor of also ~ 10, from 48 mW/cm^2 to 415 mW/cm^2. Overall, the evolution of our power densities with time are rather impressive, Figure 17, increasing by more than a factor of four in just a few months. The peak power density most recently achieved here is highly competitive with state-of-the-art fuel cells, indeed exceeding the values obtained from well-developed phosphoric acid fuel cells. A key contributor to the high power density is the impermeability of the electrolyte which results in a high open circuit voltage, 0.98 V, despite an electrolyte membrane that is only 25 μm thick. The polarization due to the electrodes, estimated as the voltage drop over the first 200 mA/cm^2 of current drawn, is 195 mV, comparable to that observed in standard PEM fuel cells.

Additional improvement of the performance of solid acid fuel cells will be achieved by further reductions in electrolyte thickness, optimization of the electrocatalyst composition and phase distribution,

and enhanced mass diffusion rate through porous stainless steel and electrocatalyst layer. However, additional reductions in electrolyte thickness beyond 25 μm, will require improvements in the mechanical properties of the electrolyte so as to provide long-term integrity of the fuel cell structure and power output. Insufficient mechanical integrity rather than processing challenges are the reason why in thinner membranes have not been examined in the period since July of 2004.

(a)   (b)
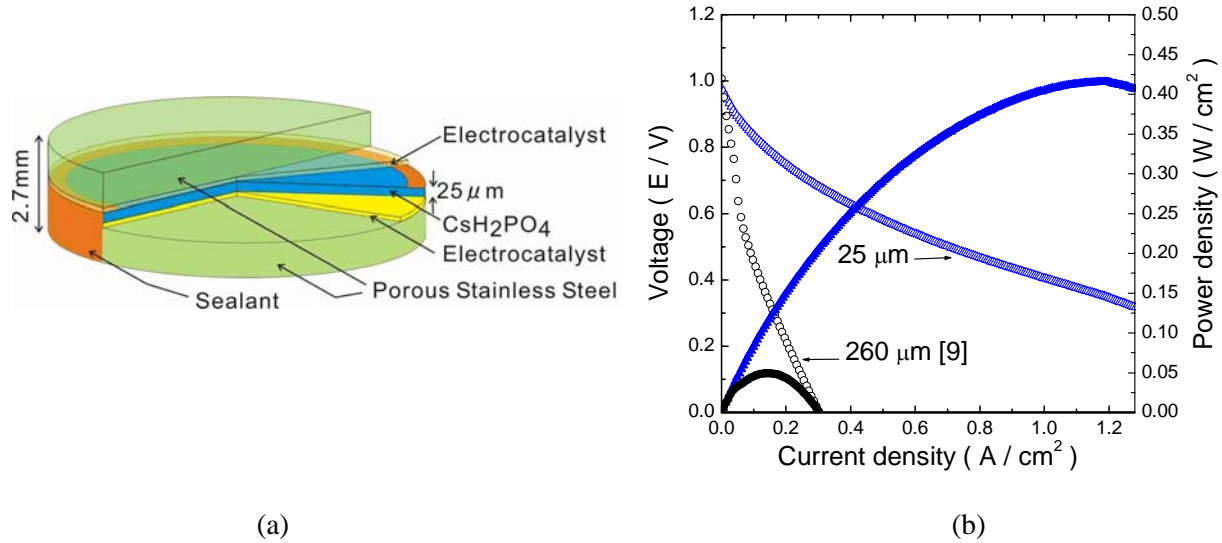
Figure 16. (a) SAFC schematic, and (b) Polarization and power density curves obtained from solid acid (CsH_2PO_4) fuel cells showing impact of electrolyte thickness on performance.
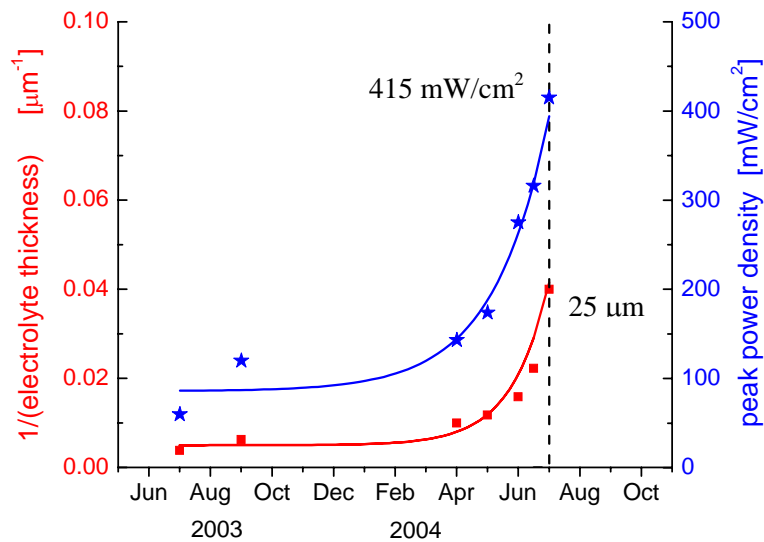
Figure 17. Evolution of SAFC fuel cell power densities as a result of reductions in membrane thickness.